Compensation for attenuation, scatter, and detector response in SPECT reconstruction via iterative FBP methods

Zhengrong Liang
Department of Radiology, Health Sciences Center, State University of New York at Stony Brook, Stony Brook, New York 11794

(Received 17 January 1992; accepted for publication 7 December 1992)

Iterative filtered backprojection (FBP) reconstruction is a fast method for single photon emission computed tomography (SPECT) that can provide simultaneous compensation for nonuniform attenuation, scatter, and distance-dependent detector response. The iterative FBP method was applied to the reconstruction of SPECT images of a chest phantom consisting of nonuniform attenuating media. One hundred twenty projections containing 20 million counts were reconstructed on an image array of $128\times128\times64$. The accuracy of reconstruction was significantly improved, in terms of concentration ratio, object shape, and noise reduction. Results of this experimental study indicate that iterative FBP can effectively reconstruct SPECT images, while other iterative methods, such as maximum *a posteriori* probability (MAP), will spend at least ten times more computing effort in the reconstruction on the same computer. The disadvantage of iterative FBP is its inability to model the noise properties of data collection accurately, as compared to the MAP methods.

Key words: emission computed tomography, thorax tomography, radionuclide imaging.

I. INTRODUCTION

Single photon emission computed tomography (SPECT) provides a useful diagnostic tool for functional imaging of the heart when used for myocardial perfusion and gated blood-pool studies.[1,2] While SPECT has been shown to produce useful images of Tc-99m-labeled radiopharmaceuticals, the quality of such studies has typically been degraded by image noise due to low count densities, and by image distortion due to (i) photon attenuation and scatter within the nonuniform attenuating media of lungs, bone, and soft tissues, and (ii) distance-dependent detector response (or spatial resolution). Although the Monte Carlo approach[3,4] can provide a unified reconstruction for SPECT which is capable of simultaneously compensating for the degradation effects, computational burden and memory requirements limit its practical application. The importance of compensating for attenuation, scatter, and detector response, and reducing image noise in clinical situations motivates this investigation on iterative filtered backprojection (FBP) reconstruction and this experimental phantom study with Tc-99m.

Iterative FBP has previously been investigated for attenuation correction in SPECT reconstruction,[5,6] and noise suppression in positron emission tomography.[7,8] The method was shown to be a reasonable approach that gave fairly good reconstructions. It has the computational advantage of fast convergence. The disadvantage is its inability to model the noise properties of data acquisition accurately, as compared to the statistical modeling method.[9,10] In the following sections, an iterative FBP algorithm for SPECT reconstruction is formulated based on a maximum *a posteriori* probability (MAP) procedure. Its reconstruction is shown to be a penalized maximum likelihood (ML) solution. The performance of the algorithm is studied by experiments on a chest phantom.

II. THEORY

The goal of image reconstruction from projections is to invert the line integrals[11] (see Fig. 1).

$$Y^p(\xi,\theta,z)=\int_{-\infty}^{\infty} O(\xi\cos\theta-\eta\sin\theta,\ \xi\sin\theta+\eta\cos\theta,z)d\eta, \tag{1}$$

for the object distribution $O(x,y,z)$, where each line integral $Y^p(\xi,\theta,z)$ is along a projection ray (say ray i) perpendicular to the z axis for a parallel-beam geometry and $O(\xi\cos\theta-\eta\sin\theta,\xi\sin\theta+\eta\cos\theta,z)$ is the representation of $O(x,y,z)$ in the rotated (detector) coordinates ξ–η–z. The rotation axis is the z axis. The ξ–z plane is the detection plane. Each line integral $Y^p(\xi,\theta,z)$ can be a measurement of photons emitted from the distribution $O(x,y,z)$ of Tc-99m-labeled radiopharmaceuticals and registered in the detector within the primary-energy window.[3–6] The inverse solution of Eq. (1) was obtained by Radon[11] (i.e., the Radon transform), and by others in different forms.[12,13]

In SPECT, where the photon absorption within the body is not negligible, the line integrals of Eq. (1) become[14]

$$Y^p(\xi,\theta,z)=\int_{-\infty}^{\infty} d\eta\, O_\theta(\xi,\eta,z)\times\exp\left(-\int_{\eta}^{\infty}\mu_\theta(\xi,\eta',z)d\eta'\right), \tag{2}$$

where $O_\theta(\xi,\eta,z)=O(\xi\cos\theta-\eta\sin\theta,\xi\sin\theta+\eta\cos\theta,z)$ and the attenuation distribution is given by the linear at-

 0094-2405/93/20(4)/1097/10/$1.20

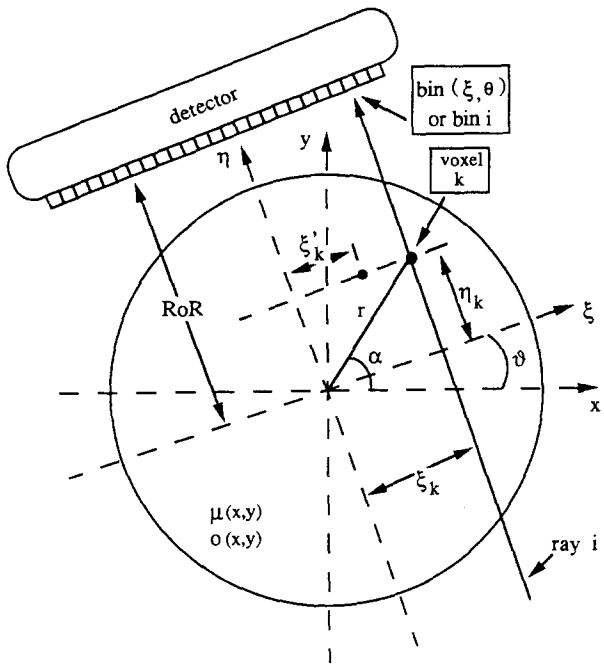

FIG. 1. The 2-D diagram of image reconstruction from projections in SPECT, and the source (stationary) and detector (rotation) coordinates.

tenuation coefficient $\mu_\theta(\xi,\eta,z)=\mu(\xi\cos\theta-\eta\sin\theta, \xi\sin\theta+\eta\cos\theta,z)$. For a constant $\mu(x,y,z)$, the inverse solution of Eq. (2) was theoretically derived in different forms as presented in Ref. 14–16 (i.e., the attenuated Radon transform). For a nonuniform $\mu(x,y,z)$, the problem of inverting the line integrals of Eq. (2) remains unsolved.

The spatial resolution of a collimator-detector system in SPECT is not constant for all source points along ray i (see Fig. 1), and is spatially invariant for those source points which are at the same distance $RoR-\eta$ (RoR is the radius of rotation) from the collimator surface. Let $C(\xi',\eta,z')$ represent the contribution weight of point (ξ',η,z') to projection bin (ξ,θ,z) on the collimator surface. Then Eq. (2) becomes[17]

$$Y^p(\xi,\theta,z)=\int_{-\infty}^{\infty}d\eta\int\int_{-\infty}^{\infty}A(\xi',\eta,z') \times C(\xi-\xi',\eta,z-z')O_\theta(\xi',\eta,z')d\xi'\,dz', \quad (3)$$

where the attenuation factor

$$A(\xi,\eta,z)=\exp\left(-\int_{\eta}^{\infty}\mu_\theta(\xi,\eta',z)d\eta'\right),$$

and the resolution function $C(\xi,\eta,z)$ can be measured for a point source in air at different distances (i.e., different η) from the collimator surface.

One may model the probability of scatter from point (ξ'',η'',z''), through multiple scatters, to point (ξ',η,z'), and then to projection bin (ξ,θ,z) by a function of $S(\xi,\eta,z,\theta,\xi',\xi'',\eta'',z',z'')$. The objective for SPECT reconstruction then becomes the inversion of the line integrals of[17]

$$\begin{aligned}Y^p(\xi,\theta,z)&=\int_{-\infty}^{\infty}d\eta\int\int_{-\infty}^{\infty}d\xi'\,dz'A(\xi',\eta,z')C(\xi-\xi',\eta,z-z')\\&\times\int\int_{-\infty}^{\infty}\int d\xi''d\eta''dz''[\delta(\xi'-\xi'',\eta-\eta'',z-z'')\\&+S(\xi,\eta,z,\theta,\xi',\xi'',\eta'',z',z'')]O_\theta(\xi'',\eta'',z''), \quad (4)\end{aligned}$$

where the scatter probability $S(\xi,\eta,z,\theta,\xi',\eta',z')$ can be determined using the Klein–Nishina formula in tracing the scatter paths from point (ξ',η',z') to bin (ξ,θ,z).[18] The product of $A\times C\times[\delta+S]$ represents the projection kernel.

It is obvious that directly inverting the line integrals of Eq. (4) is very difficult and the associated computation is very intense. Some approximations can be helpful.

Equation (4) can be rewritten as

$$\begin{aligned}Y^p(\xi,\theta,z)=&\int_{-\infty}^{\infty}d\eta\int\int_{-\infty}^{\infty}d\xi'\,dz'\,A(\xi',\eta,z')\\&\times C(\xi-\xi',\eta,z-z')O_\theta(\xi',\eta,z')+Y^s(\xi,\theta,z)\end{aligned} \quad (5)$$

where the scatter contribution to the primary-energy-window measurements, $Y^p(\xi,\theta,z)$, is given by

$$\begin{aligned}Y^s(\xi,\theta,z)=&\int_{-\infty}^{\infty}d\eta\int\int_{-\infty}^{\infty}d\xi'\,dz'\,A(\xi',\eta,z')\\&\times C(\xi-\xi',\eta,z-z')\int\int_{-\infty}^{\infty}\int d\xi''\,d\eta''\,dz''\\&\times S(\xi,\eta,z,\theta,\xi',\xi'',\eta'',z',z'')O_\theta(\xi'',\eta'',z'').\end{aligned}$$

The scatter contribution $Y^s(\xi,\theta,z)$ is the most expensive to compute. If $Y^s(\xi,\theta,z)$ can be measured approximately using dual-energy windows in data acquisition[19,20] and subtracted from the measurements of primary-energy window $Y^p(\xi,\theta,z)$, i.e., $Y(\xi,\theta,z)=Y^p(\xi,\theta,z)-Y^s(\xi,\theta,z)$, the line integrals of Eq. (5) become

$$\begin{aligned}Y(\xi,\theta,z)=&\int_{-\infty}^{\infty}d\eta\int\int_{-\infty}^{\infty}d\xi'\,dz'\,A(\xi',\eta,z')\\&\times T(\xi-\xi',\eta,z-z')O_\theta(\xi',\eta,z'),\end{aligned} \quad (6)$$

where $Y(\xi,\theta,z)$ is the scatter subtracted data and $T(\xi,\eta,z)$ is the modified $C(\xi,\eta,z)$ and includes any non-negligible effect of scatter subtraction upon the detector resolution for a point source in attenuating media. The quantity $Y(\xi,\theta,z)$ can be obtained using the dual-photo-peak window acquisition,[20] where $Y^p(\xi,\theta,z)$ is the summation of the dual-window measurements and $Y^s(\xi,\theta,z)$ is deduced from the dual-window measurements by regression. A simpler and less accurate approach to $Y(\xi,\theta,z)$ is the dual primary-scatter-window acquisition,[19] where $Y^p(\xi,\theta,z)$ is the primary-window measurement and $Y^s(\xi,\theta,z)$ is related to the scatter-window measurements $Y^s_m(\xi,\theta,z)$. If the scatter-window measurements $Y^s_m(\xi,\theta,z)$ reflect accurately the scatter portion $Y^s(\xi,\theta,z)$ in the primary-window measurements, then $Y^s(\xi,\theta,z)=Y^s_m(\xi,\theta,z)$. Otherwise, a scalar factor τ is introduced, $Y^s(\xi,\theta,z)=\tau Y^s_m(\xi,\theta,z)$, i.e., the

scatter-window measurements are assumed to be proportional to the scatter contribution in the primary-window measurements. The determination of the value τ will be discussed later.

Furthermore assume that the attenuation factor $A(\xi,\eta,z)$ varies slowly within the collimator-acceptance angle, and so the factor can be moved out from the integral of ξ',

$$Y(\xi,\theta,z)=\int_{-\infty}^{\infty} d\eta\, A(\xi,\eta,z)\int\int_{-\infty}^{\infty} d\xi' dz' \times T(\xi-\xi',\eta,z-z')O_\theta(\xi',\eta,z'), \quad (7)$$

where the convolution of detector response $T(\xi,\eta,z)$ (after scatter correction in attenuating media) with source $O(\xi,\eta,z)$ for the same η can be efficiently computed.[21]

After scatter subtraction, the line integrals of Eq. (7) lead to an efficient algorithm for computing the solution due to the convolution. Since analytical inversion of the line integrals of Eq. (7) is complicated because of the nonuniform attenuation factor $A(\xi,\eta,z)$, an alternate approach of modeling Eq. (7) in image space is considered. Equation (7) may be modeled discretely as

$$Y_i=\sum_{j=1}^{J} R_{ij}o_j, \quad i=1,2,3,...,I, \quad (8)$$

where R_{ij} is the discrete representation of the projection kernel $\{A(\xi,\eta,z)T(\xi,\eta,z)\}$, as are Y_i and o_j of $Y(\xi,\theta,z)$ and $O_\theta(\xi,\eta,z)$, respectively. The indices I and J are the total numbers of projection rays and voxels, respectively.

Theoretically, direct inversion of the transform of Eq. (8) for the solution $\{o_j\}$ is possible, given the matrix $\{R_{ij}\}$, if the data are not very noisy and the computational burden for the inversion of matrix $\{R_{ij}\}$ is not very heavy (or the matrix is not very ill posed). For SPECT imaging, because the counts are low and the size of $\{R_{ij}\}$ is very large, alternate iterative approaches to solve the solution are usually practical.

In noisy imaging situations, it is usually preferred to use a stochastic approach, rather than a deterministic approach. Based on a MAP analysis via Bayes' theorem, an iterative algorithm for the inversion of Eq. (8) has been derived:[22]

$$o_k^{(n+1)}=\bar{o}_k^{(n)}+\frac{\Sigma_i(F_{ik})(Y_i-\Sigma_j R_{ij}o_j^{(n)})}{\Sigma_i R_{ik}}, \quad (9)$$

where n is the iteration number, $\bar{o}_k^{(n)}$ is the smoothed $o_k^{(n)}$ using *a priori* specified relations between voxel k and its neighborhood, and $F_{ik}=R_{ik}\bar{o}_k^{(n)}/\Sigma_j R_{ij}o_j^{(n)}$. The smoothing may be specified in terms of either nearby voxel intensities[23] or probabilities.[24]

If neglecting the smoothing, Eq. (9) reduces to the ML reconstruction algorithm,[10] and $F_{ik}^0=R_{ik}o_k^{(n)}/\Sigma_j R_{ij}o_j^{(n)}$ is the contribution ratio of voxel k to all voxels. Furthermore if F_{ik}^0 can be approximated as a suitable low-pass filter, for example, for the Hann filter,[25] the ML algorithm resembles Chang's method[5] with $R_{ik}\approx\exp(-\mu L_{ik})$, where μ is the attenuation coefficient of the body and L_{ik} the path length from voxel k to the body boundary along ray i toward the detector (see Fig. 1). It is noted that in the backprojection step of Chang's iterative method, the attenuation factors need not be computed. This property offers the computational advantage over other iterative methods.[9,10] It is further noted that without the smoothing, the iterations of the ML and Chang's methods will not converge to an acceptable reconstruction.[22,26]

Based on the observations above, F_{ik} in Eq. (9) is heuristically assumed to be a distance-dependent kernel.[22] The function of F_{ik} is decomposed into two components: one is low-pass filtering of data in frequency space, another is distance-dependent convolution of the filtered data with $\{C_{ik}^d\}$ in image space during backprojection. The kernel T_{ik} is not used for the convolution during the backprojection, because T_{ik} is related to the attenuation map (as will be discussed later). This implementation of Eq. (9) has the computational advantage that, after filtering the data, the attenuation factors are no longer needed in the backprojection and the distance-dependent convolution in image space can be performed efficiently.

Although the formulation of Eq. (9) is based on a MAP procedure, the implementation is similar to those iterative FBP approaches,[5–8] and so the algorithm of Eq. (9) is classified as an iterative FBP method. It is clear that the iterative reconstruction of Eq. (9) converges to a penalized ML solution $\{o_j^*\}$: $\Sigma_i F_{ik}Y_i = \Sigma_i F_{ik}(\Sigma_j R_{ij}o_j^*)$, where $o_j^* = o_j^\infty$. The penalty is the smoothing for the first term on the right-hand side of Eq. (9) and the low-pass filtering for the difference in the second term.

It is noted that the low-pass filtering in frequency space and the convolution of the filtered data with C_{ik}^d at distance d in image space could be done in frequency space using a Wiener filter for that distance.[27] With the latter approach, one needs to filter the data using different Wiener filters for voxels at different distances. For example, at each projection angle, if the voxels can be arranged into 128 groups, each of which has approximately a constant distance to the collimator, then the backprojection consists of 128 loops at that angle: filter the data with a Wiener filter of distance d and backproject the filtered data to those voxels at that distance. The latter approach may need more computing time than the former, since the sizes of the kernels $\{C_{ik}^d\}$ are usually small (as shown later).

The values of $\{R_{ij}\}$ to be used for reprojection from image space to projection space are determined as follows. (It should be noted that modeling R_{ij} accurately for the reprojection is crucial for high-quality reconstruction.[17]) As shown in Fig. 1, the attenuation factor $A(\xi,\eta,z)$ from voxel k to projection bin i along ray i is given, in discrete form of Fig. 2, by

$$A_{ik}=\exp\left(-\sum_{j=1}^{k-1}\mu_j l_{ij}-\frac{1}{2}\mu_k l_{ik}\right), \quad (10)$$

where l_{ij} is the intersecting length of ray i within voxel j, and $1/2\ \mu_k/l_{ik}$ approximates the attenuation for voxel k. The lengths $\{l_{ij}\}$ are computed recursively, as shown in Fig. 2, starting at $j=1$ and ending at $j=k$ using the method described in Ref. 28 and 29.

axial direction, perpendicular to the elliptical cross section, the cylinder was 24 cm long. The lungs and bone extended the total axial length of the cylinder. In acquiring the transmission data for the nonuniform attenuation map, this "chest" phantom was filled with water. While acquiring the emission data, two "hot" spheres with thin (less than 0.1 cm thick) plastic walls were added into the chest phantom for quantification in reconstruction. The acquisition system was a three-headed SPECT system (Trionix Research Laboratory, Inc., Twinsburg, OH). The phantom has a useful feature for the testing of detector-response compensation. The two spheres and the cylinder nylon have the same diameter, but different activities and different locations. In addition the phantom has the nonuniform attenuating properties.

To obtain the nonuniform attenuation map for compensation of attenuation (i.e., to compute A_{ik}) and of scatter (i.e., to determine T_{ik}), the phantom (without the two spheres) was filled with water and scanned between an external transmission source and a detector.[30] The transmission source was Tc-99m filled in a flat plastic container. The container was mounted between two cameras of the three-headed system allowing a single head to acquire data. Approximately 42 mCi of Tc-99m in 600 ml of water filled the plastic container. A low-energy, ultra-high-resolution, parallel-hole collimator was used. The photopeak-energy window was 20% in width and centered at 140 KeV (i.e., from 126–154 KeV), the primary-emission energy of Tc-99m. Projection images of 128×128 were acquired at 120 equally spaced angles over 360° with a scan time of 20 min. The scan orbit was a circle of 46 cm in diameter. The reconstruction was done by a conventional filtered backprojection method.[25] The reconstructed attenuation map is shown on the top right of Fig. 4. The map is the summation of nine slices (each slice is 0.356 cm thick, i.e., the pixel dimension). The bottom right is the one-pixel-width profile drawn through the center of the attenuation map vertically (from A to B as indicated in the phantom diagram). The bone cannot be seen clearly because of not enough attenuation contrast between the water and the nylon. During attenuation compensation [see Eq. (10)] and construction of T_{ik} [see Eq. (11)], the attenuation map in Fig. 4 was directly used for all slices in the image array, although a segmented attenuation map may be more appropriate.[31]

The emission phantom was prepared by adding two plastic spheres inside the elliptical cylinder (see top left of Fig. 4). Note that the spheres and the "bone" have the same diameter of 2.5 cm. The spheres were filled with the same amount of Tc-99m activity (60 μCi Tc-99m in 20 ml water). The lung and the bone regions had no activity. The remaining region was filled with 6800 ml water containing 6900 μCi Tc-99m. The concentration ratio (CR) of the spheres to the "water" background was then approximately 3 to 1. The concentration profile of one pixel width through the center of the phantom is shown on the bottom left of Fig. 4. The difference in concentration between regions in the phantom simulates the isotope uptake in the activity-bearing regions. The activity-bearing regions provide a measure of the volumes, shapes and sizes of the objects, such as the spheres, bone, and lungs. Since absolute quantification of concentration in reconstruction is very complicated and depends on both source and detector system, only the CRs were considered. Since the reconstructed image density (or counts/voxel) in each activity-bearing region is proportional to the concentration in that region, the density ratios of different regions are equal to the corresponding CRs. The emission data were acquired by the three-headed system with low-energy, ultra-high-resolution, parallel-hole collimators. Although the dual photopeak-energy-window acquisition[20] could be employed for scatter compensation, the dual primary-scatter-energy-window acquisition[19] was adapted for scatter correction in this experiment. The primary-energy window was from 126–154 KeV. The scatter-energy window was from 90–126 KeV. There were 120 projections acquired equally over 360° using a scan time of 60 min. The scan orbit was an ellipse with major axis of 16.5 cm and minor axis of 12.5 cm. This scan can improve spatial resolution due to the closer distance between the detector and the body around the minor axis. The elliptical scan is not necessary for the transmission-data acquisition. Each projection was a 128×128 array. Only the center 64 axial slices were used to reconstruct an image array of $128\times128\times64$. The voxel is a cube with dimension of 0.356 cm. The counts from the primary-energy window were about 20 millions and from the scatter-energy window were approximately 14 millions.

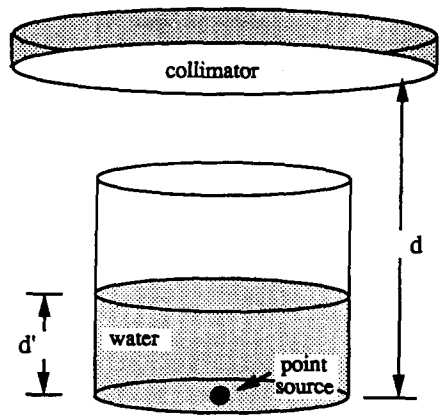

FIG. 5. The diagram for acquisition of the point-source-response function.

The Gaussian kernel T_{ik}^{d} at distance d was constructed using the dual-energy-window measurements of a Tc-99m point source ($\approx$2.5 mm in diameter) at that distance. The detector system and the dual-energy-window settings were the same as that used in acquiring the emission data. The point source was placed at the bottom center of a plastic cylindrical tank with approximately 25 cm in diameter. The collimator was on the top of the tank and at $d=5$, 10, 15, and 20 cm distances from the point source, respectively (see Fig. 5). At each distance d, water was added into the tank such that there were different water depths d' between the point source and the collimator. The scatter-window measurements were first subtracted from the primary-

TABLE I. The FWHM of detector response at different distances from collimator in air.

Distance(cm):	5	10	15	20
$FWHM_\xi$(mm):	6.6	8.3	10.3	12.8
$FWHM_z$(mm):	5.7	7.4	9.4	11.1

window measurements (with the same τ as that used for emission data subtraction) at the same distance d and the same water depth d'. Then the $FWHM_\xi$ and $FWHM_z$ of the subtracted point-source measurements were used to construct the Gaussian kernel T^d_{ik} at distance d and depth d'. The kernel at other distances d and other water depths d' were obtained by numerically fitting the measured point-source data. For $d'=0$ (i.e., no water in between), T^d_{ik} is the detector resolution in air (i.e., C^d_{ik}). The measured FWHMs in air are listed in Table I. The measured T^d_{ik} was not circularly symmetric, because the collimator–detector system was not perfectly manufactured. The $FWHM_\xi$ perpendicular to the axis of rotation was slightly larger than that parallel to the axis. For $d'\neq 0$, T^d_{ik} included the effect of scatter subtraction upon the detector resolution. This subtraction effect in water is shown in Table II below for $d=15$ cm (i.e., source–collimator distance) and for different water depths d' between the source and collimator. Similar variation of FWHM ($d'\neq 0$) about FWHM ($d'=0$) was observed for other distances $d=5$, 10, and 20 cm. The scatter-subtraction effect can be easily incorporated into the detector-response convolution by introducing an effective water depth for voxel k on ray i: $d'_{ik}=[\Sigma_j \mu_j l_{ij}+(1/2)\mu_k l_{ik}]/\mu_w$ (μ_w is the attenuation coefficient of water), for nonuniform attenuating media. For example, photons emitted from voxel k pass 5 cm air (or lung with attenuation coefficient $\mu_a=0$), 3 cm water (or soft tissues with attenuation coefficient μ_w), and 1 cm bone (with attenuation coefficient μ_b) to reach bin i, then the attenuation length $=5\mu_a+3\mu_w+\mu_b=3\mu_w+\mu_b$ and the effective depth in water $d'_{ik}=3+\mu_b/\mu_w$ cm. The effective depth bridges the difference between the resolution variations in water and in nonuniform attenuating media after scatter subtraction. The effective depth d'_{ik} is obtained when tracing the attenuation factor A_{ik} of Eq. (10), so very little computing time is needed (one division for each voxel). Once the source-collimator distance d_{ik} and the effective water depth d'_{ik} are obtained (in computing the attenuation factor A_{ik}), the detector-response kernel is then determined, the convolution of Fig. 3 for voxel k to those bins $\{i'\}$ is then straightforward.

The weighting factor τ for scatter subtraction can be estimated by a Monte Carlo simulation.[32] In this paper, τ was determined such that the tails of the point-source profiles of primary-energy window were approximately eliminated by the subtraction and $\tau=0.5$ was chosen. The low-pass filter employed in this paper was a Hann filter with rolloff parameter equal to the system Nyquist frequency (1.4 cycles per cm).

TABLE II. The FWHM of detector response for different water depths at the same distance from collimator.

depth(cm):	0	1	2	3	4	5
$FWHM_\xi$(mm):	10.3	10.0	10.0	10.5	10.4	10.4
$FWHM_z$(mm):	9.4	9.2	9.3	9.4	9.5	9.6

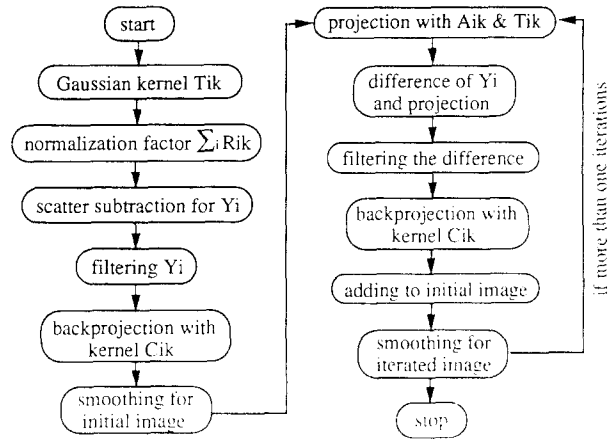

FIG. 6. The flow chart of implementing the iterative FBP algorithm.

The diagram of Fig. 6 shows the flow chart of the implementation of the iterative FBP algorithm: (1) read in the Gaussian kernels $\{T^d_{ik}\}$ and the attenuation map; (2) compute the normalization factors $\{\Sigma_i R_{ik}\}$ [see Eq. (9)] using the kernels $\{T^d_{ik}\}$ and the attenuation map [see Eq. (12)]; (3) subtract the measurements of scatter-energy window from those of primary-energy window to obtain the data $\{Y_i\}$ which are to be used to reconstruct the image; (4) transform the data $\{Y_i\}$ to the frequency space, filter them with the Hann filter, and then transform them back to the projection space; (5) backproject the filtered data, in which the convolution of the filtered data with the kernels $\{C^d_{ik}\}$ (in air) is incorporated (see Fig. 3); (6) smooth the backprojections using the nearby-voxel correlation,[23] and divide each smoothed datum k by the normalization factor $\Sigma_i R_{ik}$, then the initial image $\{o^{(0)}_k\}$ is obtained; (7) reproject the initial image using the attenuation factors $\{A_{ik}\}$ and the response kernels $\{T^d_{ik}\}$ for $\{\Sigma_j R_{ij} o^{(0)}_j\}$ [see Eq. (12)]; (8) calculate the differences between the data $\{Y_i\}$ and the projections $\{\Sigma_j R_{ij} o^{(0)}_j\}$; (9) transform the differences to the frequency space, filter them with the Hann filter, and then transform them back to the projection space [see step (4)]; (10) backproject the filtered differences in the same way as step (5) does; (11) divide the backprojected differences by the corresponding normalization factor [see Eq. (9)] and add them to the initial image; (12) smooth the modified initial image using the nearby-voxel correlation[23] for the iterated images. If more than one iteration is needed, repeat steps (7)–(12). In reconstructing the projection data of the chest phantom described above, we found out that one iteration (i.e., the 12 steps above) was enough, since further iterations (up to ten iterations) generated similar images.

The reconstruction program was coded in FORTRAN language and executed by a Stellar computer (model: GS/1000; Stardent Computer Inc., Newton, MA). It took less

ground region of the images. The errors in computing these results in this phantom study are comparable, since the same method was used to determine the ROI for each object (see Sec. III). The variance in the estimation can be computed with more phantom studies. The computed volumes for the central sphere were not consistent with visual judgement on the Figs. 8 and 9. This inconsistency is due to the much lower background at the central area of the uncompensated image, as compared to that of the compensated image. It is noted that the detector-response compensation improves the resolution of the reconstruction while, at least, preserving the SNR of the result. The significance of the detector-response compensation lies in the improvement of the object-shape reconstruction. The compensation compressed the distorted hot and cold regions of the two spheres and the bone (see Figs. 8 and 9) into circular regions and improved the object volumes closer to the true object size.

The above comparisons were performed using the FBP-type reconstructions. The filter and projectors were the same for all the reconstructions except for the different compensations. The computational costs of this algorithm for different compensations were similar for all the iterative FBP methods.[5–8] Since the iterative FBP reconstruction of Eq. (9) is a penalized ML solution, a comparison between MAP and this iterative FBP reconstruction would be useful. As reported in Refs. 35 and 36, the iterative FBP reconstruction was better for the cold objects (i.e., the bone and lungs), worse for the hot objects (i.e., the two spheres), and comparable for the background, as compared to the MAP reconstruction.[34]

V. DISCUSSION

The iterative FBP, a modified and unified reconstruction method for SPECT, has been shown to provide satisfactory images for phantom scans in a practical situation. The compensation for nonuniform attenuation and scatter within the chest phantom and for distance-dependent detector response is effective. Qualitative improvement in identifying object shape and size in the reconstructed images is observed. Quantitative improvement on concentration ratio, object volume, and noise reduction is obtained.

The computation time required to generate satisfactory images with the iterative FBP is at least ten times less than the iterative ML and MAP reconstructions. The latter approaches usually need more than 20 iterations, while the former method requires computation time equivalent to 2 iterations of the latter approaches. The FORTRAN code of the iterative FBP algorithm was executed on a Stellar computer model GS/1000 with less than 4 h for $128\times128\times64$ array from 120 projections. With SUN Sparc stations 2 or 10, the computation time can be easily reduced to less than an hour. Further reduction in computation time can be obtained by parallelizing the program code.

The computer coding of the iterative FBP is relatively easy. The process of filtering is identical to that of the conventional FBP.[25] The attenuation compensation factors or normalization factors $\{\Sigma_i R_{ik}\}$ are computed in a manner similar to Chang's method.[5] The subtraction of dual-energy-window data is straightforward, a simple modification of Jaszczak's method.[19] The convolution technique is well documented.[21]

It is noted that the convolution improves significantly the object shape and SNR, while preserving the object contrast within the phantom in this experimental study. This gain with detector-response compensation was also indicated in Ref. 37. The convolution approach can be applied to the distance-dependent detector response, positron and angular range blurring in positron emission tomography.[38,39]

It is clear that the application of the iterative FBP method to clinical studies requires an efficient reconstruction of the nonuniform attenuation map of the body (see Fig. 4). Two approaches have been simulated to improve the reconstruction of the attenuation map.[40] In the first approach, an external line source was employed to generate the transmission data using a three-headed SPECT system. The emission data were acquired after injection following the transmission scan. The attenuation map was simultaneously reconstructed and segmented, given the transmission data and the attenuation coefficients of bone, lungs, soft tissues, and air.[41] In the second approach, the attenuation map was constructed by fitting the attenuation coefficients to the segmented magnetic resonance (MR) image if the patient had a MR scan available.[42]

ACKNOWLEDGMENTS

The authors are grateful to Dr. D. Gilland and Mr. K. Greer for their assistance in data acquisition, and Dr. R. Jaszczak, Dr. E. Coleman, Dr. T. Turkington, and Dr. G. Gindi for their assistance in preparing this manuscript. This investigation was supported by Grant No. HL44194, awarded by the National Heart, Lung, and Blood Institute.

[1]L. C. Becker, "Myocardial perfusion," in *Textbook of Nuclear Medicine Volume II: Clinical Applications* (Lea & Febiger, Philadelphia, 1984), pp. 383–405.
[2]M. L. Stadius and J. L. Ritchie, "Gated blood pool tomography," in *New Concepts in Cardiac Imaging* (Year Book Medical, Chicago, 1986), pp. 137–154.
[3]J. W. Beck, R. J. Jaszczak, R. E. Coleman, C. F. Starmer, and L. W. Nolte, "Analysis of SPECT including scatter and attenuation using sophisticated Monte Carlo modeling methods," IEEE Trans. Nucl. Sci. **29**, 506–511 (1982).
[4]C. E. Floyd, R. J. Jaszczak, K. L. Greer, and R. E. Coleman, "Inverse Monte Carlo as a unified reconstruction algorithm for ECT" J. Nucl. Med. **27**, 1577–1585 (1986).
[5]C. T. Chang, "A method for attenuation correction in radionuclide computed tomography," IEEE Trans. Nucl. Sci. **25**, 638–643 (1978).
[6]T. E. Waters, W. Simon, D. A. Chesler, and J. A. Correia, "Attenuation correction in gamma emission computed tomography," J. Comput. Assist. Tomogr. **5**, 89–94 (1981).
[7]E. Tanaka, "A filtered iterative reconstruction algorithm for positron emission tomography," Inf. Process. Med. Imag. **10**, 217–233 (1988).
[8]E. Tanaka, "Intelligent iterative image reconstruction with automatic noise artifact suppression," Proc. IEEE Med. Imag. **2**, 1480–1486 (1990).
[9]A. J. Rockmore and A. Macovski, "A maximum likelihood approach to emission image reconstruction from projections," IEEE Trans. Nucl. Sci. **23**, 1428–1432 (1976).
[10]L. A. Shepp and Y. Vardi, "Maximum likelihood reconstruction for emission tomography," IEEE Trans. Med. Imag. **1**, 113–122 (1982).

[11]J. Radon, "Uber die Bestimmung von Funktionen durch ihre Integralwerte langs gewisser Mannigfaltigkeiten," Akad. Wiss. Leipzig Math. Phys. Kl. Ber. **30**, 262–277 (1917).
[12]A. M. Cormack, "Representation of a function by its line integrals with some applications," J. Appl. Phys. **34**, 2722–2727 (1963).
[13]L. A. Shepp and B. F. Logan, "The Fourier reconstruction of a head section," IEEE Trans. Nucl. Sci. **21**, 21–43 (1974).
[14]G. T. Gullberg, "The attenuated radon transform: Theory and application in medicine and biology," Ph.D. thesis, University of California, Berkeley, CA, 1979.
[15]A. Bellini, M. Piacentini, C. Cafforio, and F. Rocca, "Compensation of tissue absorption in emission tomography," IEEE Trans. ASSP. **27**, 213–218 (1979).
[16]O. Tretiak and C. E. Metz, "The exponential radon transform," SIAM J. Appl. Math. **39**, 341–354 (1980).
[17]Z. Liang, R. J. Jaszczak, C. E. Floyd, K. L. Greer, and R. E. Coleman, "Reprojection and backprojection in SPECT image reconstruction," Proc. IEEE Energ. Inform. Tech. Southeast. **2**, 919–926 (1989).
[18]J. H. Hubbell, W. J. Veigele, E. A. Briggs, R. T. Brown, D. T. Cromer, and R. J. Howerton, "Atomic form factors, incoherent scattering functions, and photon scattering cross sections," J. Phys. Chem. Ref. Data **4**, 471–538 (1975).
[19]R. J. Jaszczak, K. L. Greer, C. E. Floyd, C. C. Harris, and R. E. Coleman, "Improved SPECT quantification using compensation for scattered photons," J. Nucl. Med. **25**, 893–900 (1984).
[20]M. A. King, G. J. Hademenos, and S. J. Glick, "A dual photo-peak window method for scatter correction," J. Nucl. Med. **33**, 605–612 (1992).
[21]H. J. Nussbaumer, *Fast Fourier Transform and Convolution Algorithms* (Springer, New York, 1981).
[22]Z. Liang, "Implementation of linear filters for iterative penalized maximum likelihood SPECT reconstruction," IEEE Trans. Nucl. Sci. **38**, 606–611 (1991).
[23]Z. Liang, R. J. Jaszczak, C. E. Floyd, and K. L. Greer, "A spatial interaction model for statistical image processing," Inf. Process. Med. Imag. **11**, 29–43 (1989).
[24]J. Besag, "Spatial interaction and the statistical analysis of lattice system," J. R. Stat. Soc. B **36**, 192–236 (1874).
[25]R. H. Huesman, G. T. Gullberg, W. L. Greenberg, and T. F. Budinger, *Donner Algorithms for Reconstruction Tomography* (Lawrence Berkeley Laboratory, University of California, 1977).
[26]D. L. Snyder, M. I. Miller, L. J. Thomas, and D. G. Politte, "Noise and edge artifacts in maximum-likelihood reconstructions for emission tomography," IEEE Trans. Med. Imag. **6**, 228–238 (1987).
[27]M. A. King, R. B. Schwinger, P. W. Doherty, and B. C. Penney, "Two-dimensional filtering of SPECT images using the Metz and Wiener filters," J. Nucl. Med. **25**, 1234–1240 (1984).
[28]R. L. Siddon, "Fast calculation of the exact radiological path for a three-dimensional CT array," Med. Phys. **12**, 252–255 (1985).
[29]S. H. Manglos, R. J. Jaszczak, C. E. Floyd, L. J. Hahn, K. L. Greer, and R. E. Coleman, "Nonisotropic attenuation in SPECT: Phantom tests of quantitative effects and compensation techniques," J. Nucl. Med. **28**, 1584–1591 (1987).
[30]D. R. Gilland, R. J. Jaszczak, T. G. Turkington, K. L. Greer, and R. E. Coleman, "Quantitative SPECT imaging with Indium-111," IEEE Trans. Nucl. Sci. **38**, 761–766 (1991).
[31]Z. Liang, R. J. Jaszczak, and R. E. Coleman, "Parameter estimation of finite mixtures for image processing using the EM algorithm and information criteria," Proc. IEEE Med. Imag. **3**, 2171–2178 (1992).
[32]M. F. Smith, C. E. Floyd, R. J. Jaszczak, and R. E. Coleman, "Evaluation of projection pixel-dependent and pixel-independent scatter correction in SPECT," Proc. IEEE Med. Imag. **3**, 1782–1788 (1992).
[33]Z. Liang, R. J. Jaszczak, C. E. Floyd, K. L. Greer, and R. E. Coleman, "Bayesian reconstruction of SPECT in parallel, fan, and cone beam geometries," J. Nucl. Med. **29**, 871 (1988).
[34]Z. Liang, T. G. Turkington, D. R. Gilland, R. J. Jaszczak, and R. E. Coleman, "Simultaneous compensation for attenuation, scatter, and detector response for SPECT reconstruction in three dimensions," Phys. Med. Biol. **37**, 587–603 (1992).
[35]Z. Liang, "Compensation of non-uniform attenuation, scattering, and collimator response with an iterative FBP method for SPECT reconstruction," Radiology **181**, 186 (1991).
[36]Z. Liang, "An efficient three-dimensional unified projector-backprojector for SPECT reconstruction," Proc. IEEE Med. Imag. **3**, 1975–1979 (1992).
[37]G. L. Zeng and G. T. Gullberg, "Three-dimensional iterative reconstruction algorithms with attenuation and geometric point response correction," IEEE Trans. Nucl. Sci. **38**, 693–702 (1991).
[38]G. Muehllehner and J. S. Karp, "Positron emission tomography imaging—Technical considerations," Semin. Nucl. Med. **16**, 35–50 (1986).
[39]S. F. Haber, S. E. Derenzo, and D. Uber, "Application of mathematical removal of positron range blurring in PET," IEEE Trans. Nucl. Sci. **37**, 1293–1299 (1990).
[40]Z. Liang, "Reconstruction of non-uniform attenuation map for quantitative emission computed tomography," submitted to Ann. Meeting of SNM (1993).
[41]Z. Liang, R. J. Jaszczak, R. E. Coleman, and V. E. Johnson, "Simultaneous reconstruction, segmentation, and edge enhancement of relatively piecewise continuous images with intensity-level information," Med. Phys. **18**, 394–401 (1991).
[42]Z. Liang and J. R. MacFall, "Parameter estimation and NMR image segmentation," presented at Ann. Meeting of IEEE Med. Imag. (1992).